Supporting Information

Single-Crystal Rutile TiO_2 Nanocylinders are Highly Effective Transducers of Optical Force and Torque

Seungkyu Ha, Ying Tang, Maarten M. van Oene, Richard Janissen, Roland M. Dries, Belen Solano, Aurèle J. L. Adam, and Nynke H. Dekker

Supporting Text

Supporting Figures

Supporting Tables

Supporting References

Supporting Text

Text S1. Derivation of the analytical equation for optical torque transfer from a linearly polarized plane wave to an infinitely wide birefringent plate with uniform thickness.

The purpose of this section is to confirm the validity of eq 1, as in the literature many different forms of this equation exist in the absence of detailed derivation.[1–4] First, we start with torque on a single dipole in a plate

$$\vec{\tau} = \vec{p} \times \vec{E}, \tag{S1}$$

where $\vec{p}$ is the electric dipole moment and $\vec{E}$ is the electric field in the plate.[5] We can derive the torque per unit volume of a dielectric plate of uniform thickness perpendicular to the beam propagation direction by considering multiple dipoles in a given volume

$$N\vec{\tau} = N\vec{p} \times \vec{E} = \vec{P} \times \vec{E} = \varepsilon_o \underline{\chi} \vec{E} \times \vec{E}, \tag{S2}$$

where N is the number of dipoles, $\vec{P}$ is the polarization per unit volume, ε_o is the vacuum permittivity, and $\underline{\chi}$ is the electric susceptibility tensor in the plate. The input beam is set to be a plane wave that propagates in the z-direction, being linearly polarized in xy-plane. Thus, the electric field $\vec{E}$ has zero intensity in the z-dimension ($E_z = 0$) and hence torque is applied in the z-direction only

$$N\vec{\tau} = \varepsilon_o \begin{bmatrix} \chi_x & 0 & 0 \\ 0 & \chi_y & 0 \\ 0 & 0 & \chi_z \end{bmatrix} \begin{bmatrix} E_x \\ E_y \\ 0 \end{bmatrix} \times \begin{bmatrix} E_x \\ E_y \\ 0 \end{bmatrix} = \varepsilon_o \begin{bmatrix} 0 \\ 0 \\ (\chi_x - \chi_y) E_x E_y \end{bmatrix}. \tag{S3}$$

Using the known relationship $\chi = n^2 - 1$, the torque in the z direction can be described as

$$N\tau_z = \varepsilon_o (\chi_x - \chi_y) E_x E_y = \varepsilon_o (n_x^2 - n_y^2) E_x E_y. \tag{S4}$$

In eq S4, the electric field vectors (E_x, E_y) in time t and space z are defined as

$$\begin{aligned} E_x &= E_x(z,t) = E_{0,x} \cos(k_x z - \omega t), \\ E_y &= E_y(z,t) = E_{0,y} \cos(k_y z - \omega t), \end{aligned} \tag{S5}$$

where $E_{0,x} = E_0 \cos(\theta)$, $E_{0,y} = E_0 \sin(\theta)$, and θ is the angle between the x-axis and the linear polarization direction of the electric field with amplitude E_0 in the plate. Also, $k_x = k_0 n_x$, $k_y = k_0 n_y$, while n_x, n_y are refractive indices of the plate along the x- and y-axis, k_x, k_y are wavenumbers in the plate along the x- and y-axis, and $k_0 = \frac{\omega}{c}$ is the wavenumber in vacuum (here, ω is the laser optical frequency and c is the speed of light in vacuum). We rewrite eq S5 similarly to Beth's derivation[1]

$$\begin{aligned} E_x(z,t) &= E_{0,x} \cos\left(\tfrac{k_x + k_y}{2} z + \tfrac{k_x - k_y}{2} z - \omega t\right) = E_{0,x} \cos(Z + D), \\ E_y(z,t) &= E_{0,y} \cos\left(\tfrac{k_x + k_y}{2} z - \tfrac{k_x - k_y}{2} z - \omega t\right) = E_{0,y} \cos(Z - D), \end{aligned} \tag{S6}$$

where $Z = kz - \omega t$ and $D = \frac{\Delta k}{2} z$ (here, $k = \frac{k_x + k_y}{2}$, $\Delta k = k_x - k_y = k_0 (n_x - n_y) = k_0 \Delta n$). Using trigonometric identities, we can further simplify the factor $E_x E_y$ in eq S4. This allows us to express the z-component of the instantaneous torque per unit volume as

$$N\tau_z = \varepsilon_o\left(n_x^2 - n_y^2\right)E_xE_y = \frac{\varepsilon_o\left(n_x^2-n_y^2\right)E_0^2}{4} sin(2\theta)\,(cos(2Z) + cos(2D)), \quad \text{(S7)}$$

and its time-averaged variant as

$$\langle N\tau_z\rangle = \frac{1}{T}\int_0^T dt\, N\tau_z = \frac{\varepsilon_o\left(n_x^2-n_y^2\right)E_0^2}{4} sin(2\theta)\, cos(z\Delta k). \quad \text{(S8)}$$

To obtain the torque per unit area for a given plate thickness (i.e., height) h, we integrate along the z-axis

$$\int_0^h dz\,\langle N\tau_z\rangle = hN\langle\tau_z\rangle = \frac{\varepsilon_o\left(n_x^2-n_y^2\right)E_0^2}{4} sin(2\theta)\left(\frac{1}{\Delta k}[sin(z\Delta k)]_0^h\right)$$

$$= \frac{\varepsilon_o c\left(n_x^2-n_y^2\right)E_0^2}{4\omega\Delta n} sin(2\theta)\, sin(h\Delta k) = \frac{\varepsilon_o ncE_0^2}{2\omega} sin(2\theta)\, sin(hk_0\Delta n), \quad \text{(S9)}$$

where n is the mean index (i.e., $n = \frac{n_x+n_y}{2}$) of the plate. Finally, the torque per plate volume can be obtained by rewriting $N = \frac{N_d}{V} = \frac{N_d}{hS}$, where N_d is the total number of dipoles within the plate and S is the area of the plate surface with which the beam interacts

$$\langle\tau_{z,total}\rangle = N_d\langle\tau_z\rangle = \frac{S\varepsilon_o ncE_0^2}{2\omega} sin(hk_0\Delta n)\, sin(2\theta), \quad \text{(S10)}$$

which is identical to the amplitude of torque in eq 1 in the main text. We note that this equation is derived under the idealized condition of a plane wave interacting only with an infinitely wide plate of uniform thickness. It does not take into account the surrounding medium, and as such, the accompanying reflections at the material interfaces. When we use such idealized conditions in our FEM calculations, we obtain results identical to those predicted by eq 1 (Supporting Information, Figure S10; although a plate of finite size, e.g., 300 nm × 300 nm surface area, is required by FEM models, it is equivalent to the infinite case when light diffraction near the plate edges is ignored). Therefore, torque values acquired under non-ideal but realistic conditions deviate from the predictions of eq 1. As further detailed in Supporting Information, Figure S1, one such example is a particle with a finite size trapped by a tightly-focused beam, e.g., rutile TiO_2 nanocylinder trapping experiments in OTW as shown in Figure 1e.

Text S2. Potential crosstalk between translational and rotational degrees of freedom of an optically trapped birefringent nanocylinder.

The potential origins of crosstalk between force and torque of an optically trapped birefringent nanocylinder are discussed here. First, physical correlations between translational and rotational degrees of freedom will occur because the rutile TiO_2 cylinders exhibit both optical and geometrical anisotropy, and this will influence their dynamics within a tightly focused beam. For example: (i) if a large external axial torque is applied on a nanocylinder while the trapping beam linear polarization direction is fixed, then the particle will be rotated with a large offset angle around the *z*-axis. Therefore, there will be noticeable change in forces along the *x*- and the *y*-axis due to both the particle birefringence and the elliptical beam shape of the focus beam (originated from its linearly polarized state at large NA of the objective lens); (ii) if a nanocylinder has a large lateral displacement from the trap center, then the overlap between the cylinder volume and the focal volume will be decreased and hence the achievable maximum force and torque will be smaller due to the reduced light–matter interaction; and (iii) if a nanocylinder is tethered to the flow cell bottom through a linker (e.g., a single biomolecule such as a DNA strand) and a lateral force is applied, then a lateral torque will rotate the nanocylinder around one of the lateral axes. As a result, all the forces (along *x*, *y*, and *z*-axis) and the torques (about *x*, *y*, and *z*-axis) will be changed as a function of the angle offset.

Second, the crosstalk between the detection channels of force and torque exists even in the absence of the abovementioned physical correlations. The force is detected via a position sensitive detector (PSD; *x*, *y*) and a photodiode (PD: *z*) (alternatively, a PSD or a quadrant photodiode (QPD) for detection of all *x*, *y*, and *z*), while the torque is detected by two dedicated PDs. When the torque (and hence the output beam polarization) changes, the polarization-dependent responsivity of PSD and PD can result in crosstalk to the force signal. Similarly, when the particle's lateral position changes, the deflection of the output beam can result in a non-optimal alignment of the beam path towards the two PDs and affect the torque measurements.

In practice, the characterization of such crosstalk can be more complicated because the physical correlations themselves can also affect the force and torque detection. For example, in the measurement of a cylinder position (and hence force), the PSD signal is affected by the two lateral tilt angles of the cylinder,[6] unlike the signal from a spherical particle for which tilting does not affect the PSD signal. However, in the measurements presented in this manuscript, such complex crosstalk can be neglected as the tilting about the lateral axes are suppressed and therefore the major part of the PSD signal is still translational information only (i.e., the linear calibration is valid). The rotation of a nanocylinder around the lateral axes is constrained by both restoring torque components arising from material birefringence and cylindrical geometry, as shown by our numerical calculations shown in Supporting Information, Figure S3. Also, by using higher laser beam power, such unwanted lateral rotation can be suppressed further by the increased strength of the restoring torques. We used the highest beam power (~92 mW) allowed in our setup for measuring linear stiffness. Even during the force calibration using the sinusoidal modulation method,[7] the induced lateral tilts are also negligible due to the small amplitude of the particle's sinusoidal movement, which is much smaller than that of the thermal fluctuation[7]: in our experiments, the sinusoidal modulation of the piezo stage (on which the flow cell is mounted) for such condition has amplitude of 25-75 nm at 40 Hz. Ideally, the measurement of nanocylinder translation and rotation will become more accurate in diverse experimental configurations if the two lateral tilting angles (around the *x*- and *y*-axes when the laser beam propagates along the *z*-axis) can be precisely measured simultaneously in addition to the three-dimensional displacements (*x*, *y*, and *z*), enabling 5D-tracking.[6]

Supporting Figures

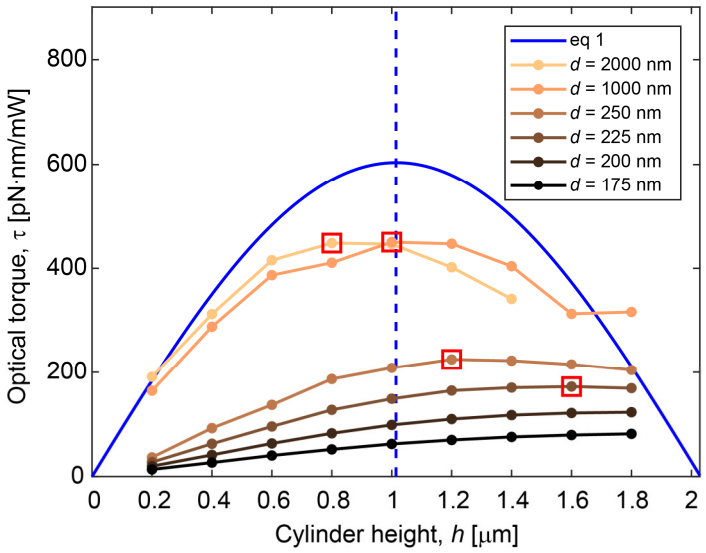

Figure S1. FEM-calculated rutile TiO_2 nanocylinder height for maximal torque transfer efficiency at different fixed diameters. The maximal optical torque (filled circles) of rutile TiO_2 nanocylinders as a function of their height (h = 0.2–1.8 μm) for different diameters (d = 175–2000 nm), FEM-calculated at z_{eq} = 0 nm and θ = 45° (for the largest diameter d = 2000 nm, calculation is performed up to h = 1.4 μm due to the limitation of computing memory). Calculations are performed assuming a focus beam with the vacuum wavelength λ_o = 1064 nm, objective lens NA = 1.2, an objective lens filling ratio $\alpha = \infty$, and a surrounding medium index n = 1.33. For comparison, the analytical prediction (blue curve, using eq 1 from the main text) assuming a plane wave interacting with a rutile TiO_2 plate of 300 nm × 300 nm surface area is coplotted. The vertical dashed blue line ($h \approx 1$ μm) indicates the analytical prediction of optimal cylinder height for the maximal torque transfer efficiency, while the numerical predictions are designated by red squares if they exist within the calculated range. Note that nanoparticles with diameters smaller than the beam wavelength (d = 175–250 nm) deviate most from the analytical prediction. Cylinders with diameters comparable to or larger than the beam wavelength (d = 1000–2000 nm) show optical torque that more closely approximates the analytical prediction, as their geometry is closer to that of a rutile TiO_2 plate.

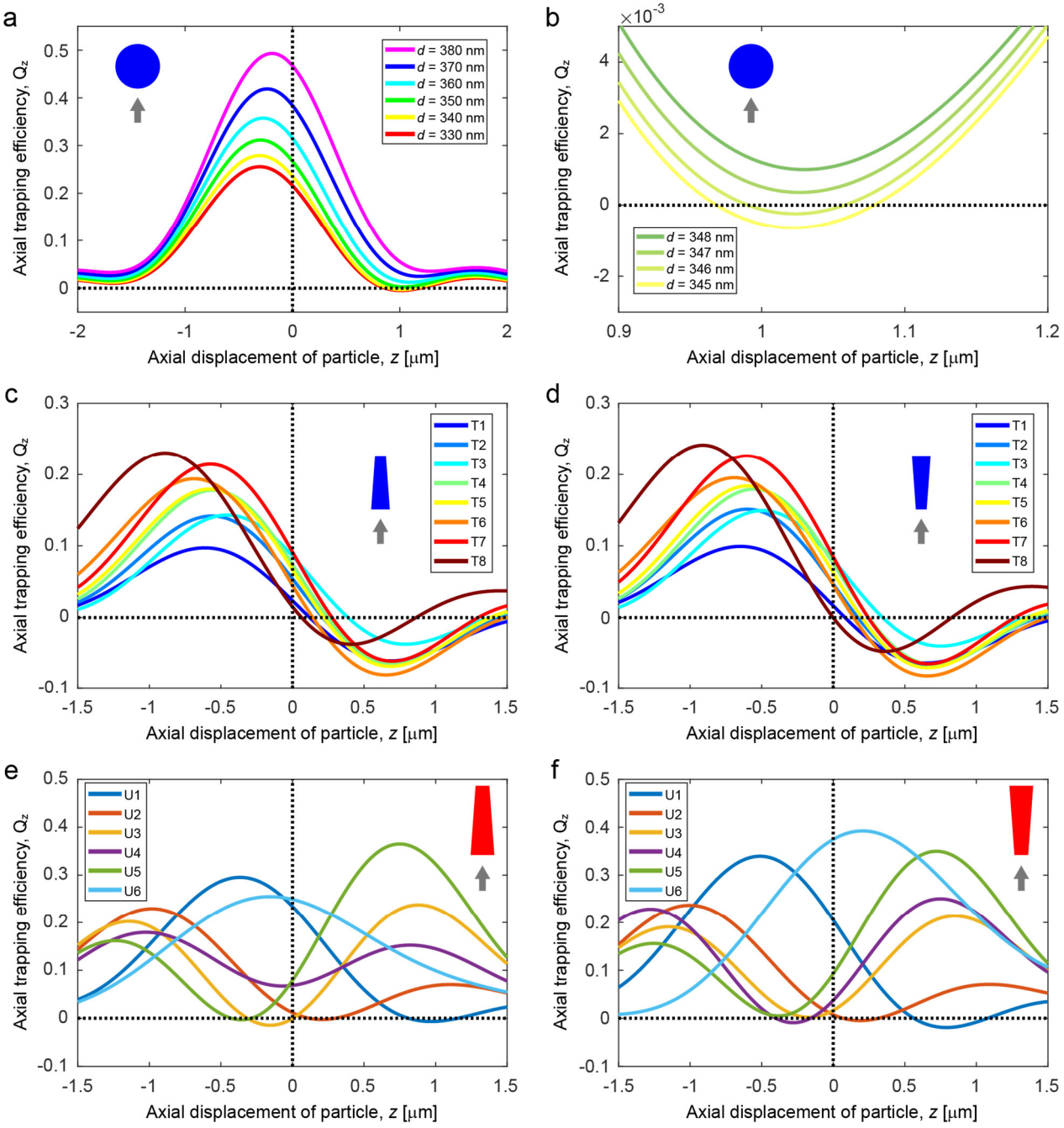

Figure S2. FEM-calculated optical trappability of rutile TiO_2 spheres and cylinders. (a) The FEM-calculated axial trapping efficiency (Q_z) curves (i.e., normalized axial force (F_z) curves; $Q_z = F_z/(nP/c)$, where n is the refractive index of the surrounding medium, P is the trapping laser beam power, and c is the speed of light in vacuum) for rutile TiO_2 spheres with diameters of 330–380 nm, demonstrating that spheres with large volume (≥ ~350 nm) are not trappable. (b) FEM-calculations of Q_z with 1 nm-step in sphere diameter (345–348 nm) reveal that the diameter of the largest trappable rutile TiO_2 sphere is ~346 nm. (c–f) The FEM-calculated axial trapping efficiency (Q_z) curves for all fabricated rutile TiO_2 nanocylinder batches, using average SEM-measured dimensions with actual sidewall profiles as input parameters. The trap strengths (as defined in Supporting Information, Figure S5) of trappable cylinders (T1–T8; (c, d)) are much larger than those of non-trappable cylinders (U1–U6; (e, f)). As the cylinders are not symmetric in the z-dimension, two different trapping orientations exist for each cylinder (with the positive (c, e) or negative (d, f) taper angle with respect to the input beam as shown in the inset diagram). For trappable cylinders (T1–T8; (c, d)), as their taper angles are small (0.1–1.6°, Supporting Information, Table S1), the trapping orientation does not significantly contribute to trapping behavior (Supporting Information, Figure S6). All calculations in panels (a)–(f) are performed assuming a focus beam with objective lens NA = 1.2, an objective lens filling ratio α = 1.7, and a surrounding medium index n = 1.33.

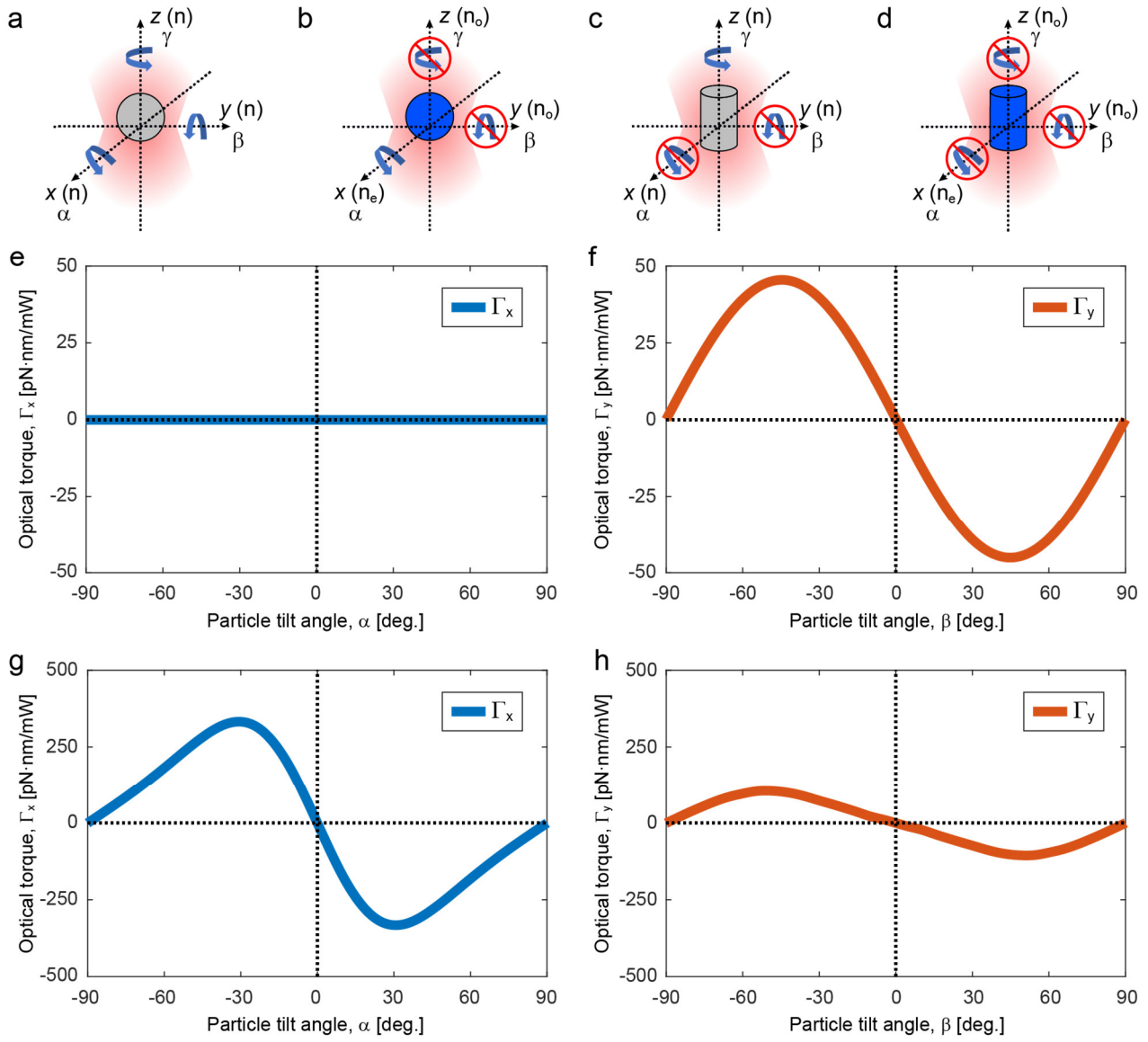

Figure S3. FEM-calculated RDOF confinement torque of rutile TiO_2 spheres and cylinders. Visual representation of the mechanism of RDOF confinement, supported by numerical calculations. (a–d) Illustrations of achievable confinement of the RDOF depending on the degree of geometrical or optical anisotropy. An optically isotropic particle (gray, e.g., polystyrene) has a constant refractive index (n) along its principal axes (x, y, and z), while a birefringent particle (blue, e.g., rutile TiO_2) includes an extraordinary index (n_e) that differs from the other two ordinary indices (n_o). Here, a positively birefringent crystal (e.g., rutile TiO_2) is assumed, and thus $n_e > n_o$. A blue curved arrow indicates free rotation in the absence of confinement, while an overlaid prohibitory traffic sign indicates the restriction in rotation due to the confined RDOF. The incident trapping beam is assumed to be linearly polarized in the x-dimension. (a) A non-birefringent sphere, which is fully isotropic, has no confined RDOF. (b) A positively birefringent sphere that has optical anisotropy only, has two confined RDOF. (c) A non-birefringent cylinder that has geometrical anisotropy only, has two confined RDOF. (d) A positively birefringent cylinder, which is fully anisotropic, has fully confined RDOF. (e, f) FEM-calculated optical torque components for a positively birefringent sphere (rutile TiO_2, d = 150 nm), i.e., configuration in panel (b). The result shows that indeed the angle α is not confined, as (e) Γ_x remains zero at any angle, while the angle β is confined by the restoring torque (f) Γ_y from the optical birefringence. (g, h) FEM-calculated optical torque components for a positively birefringent cylinder (rutile TiO_2, d = 200 nm and AR = 5), i.e., configuration in panel (d). The confinement in the angle α results from the restoring torque (g) Γ_x generated by the uneven radiation pressure distribution on a tilted cylinder (no such geometrical effect would occur in the case of a tilted sphere). The angle β is doubly confined by the restoring torque (h) Γ_y from both geometrical and optical anisotropy. The confinement of the RDOF in the angle γ by the restoring torque Γ_z that results from particle birefringence is common to both sphere and cylinder. All calculations in panels (e)–(h) are performed assuming the vacuum wavelength of input beam λ_o = 1064 nm, an equilibrium axial trapping position z_{eq} = 0, a focus beam with objective lens NA = 1.2, an objective lens filling ratio $\alpha = \infty$, and a surrounding medium index n = 1.33.

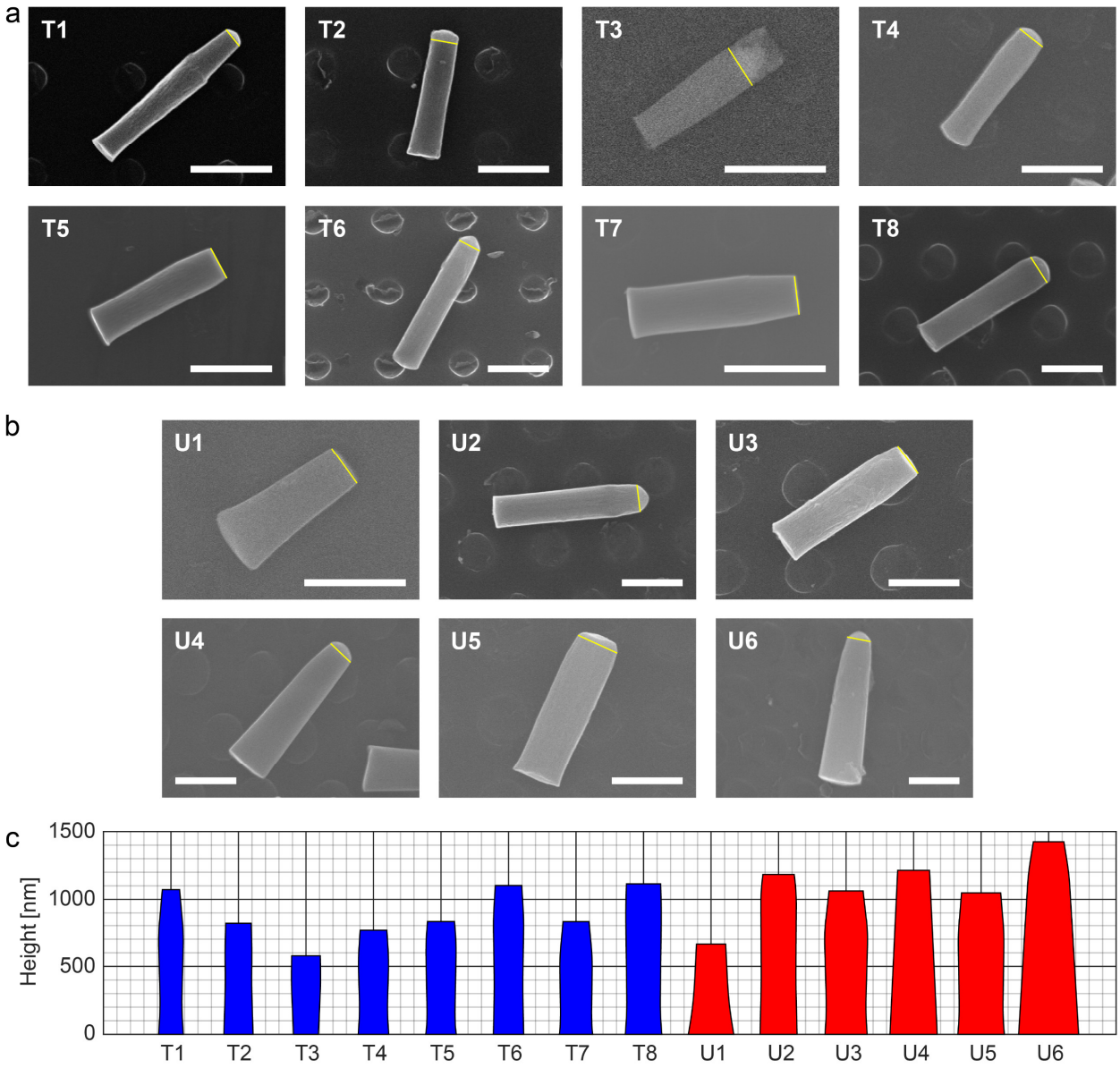

Figure S4. SEM micrographs of top-down fabricated single-crystal rutile TiO_2 nanocylinder batches. (a, b) A representative SEM micrograph of each cylinder batch is shown: (a) trappable nanocylinder batches (T1–T8); (b) untrappable nanocylinder batches (U1–U6). All scale bars are 500 nm. The yellow lines indicate the top surfaces of cylinders, and the structures (mostly in a hemispherical or a disk shape) just above them are Cr masks that remain when SEM images are taken prior to Cr removal by wet etching (except the images of T5, T7, U1, and U3). Optical trapping experiments are performed only after the complete removal of Cr masks. Otherwise, stable optical trapping is hindered due to the large scattering from the Cr layer. (c) Geometries of trappable (blue) and untrappable (red) nanocylinders drawn up on the same scale with the mean dimensions obtained from multiple SEM images (Supporting Information, Table S1). Both vertical and horizontal grid lines have the same spacing (100 nm-step for thin lines and 500 nm-step for thick lines).

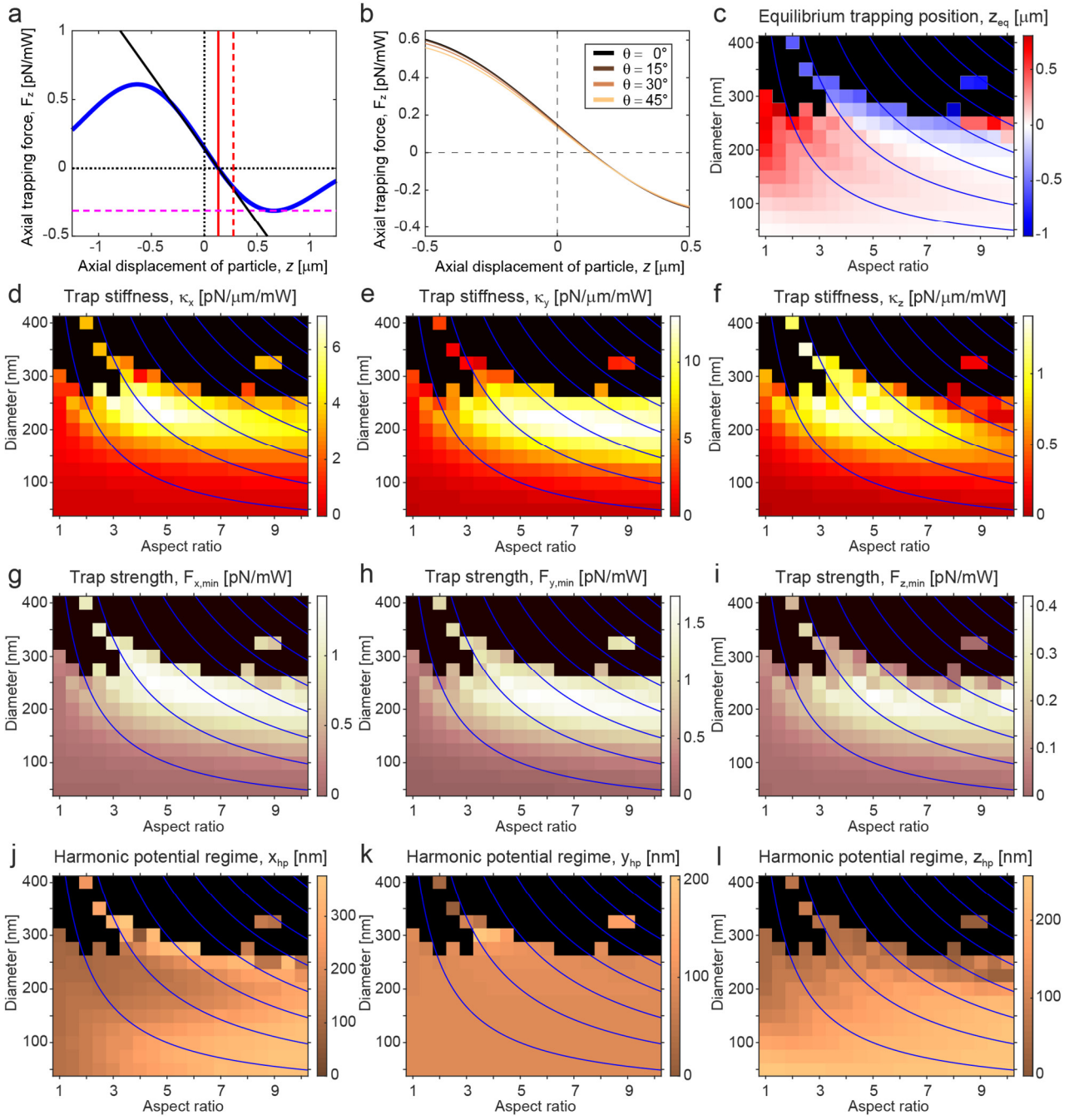

Figure S5. FEM-calculated parameters describing the linear optical trapping behavior of rutile TiO_2 nanocylinders. Linear trapping parameters deduced from FEM-calculated force curves, plotted as a function of cylinder diameter and aspect ratio. (a) The definitions of these parameters are graphically summarized with an axial force curve (the blue curve, for a nanocylinder with d = 200 nm and AR = 5 as an example): the axial equilibrium trapping position z_{eq} (the vertical red line which is the x-intercept of the force curve), the axial trap stiffness κ_z (the gradient of force at z_{eq} designated by the solid black tangential line which approximates the harmonic potential well), the axial trap strength $F_{z,min}$ (the horizontal magenta dashed line over which the particle will escape from the trap), and the axial harmonic potential regime z_{hp} (the distance from z_{eq} to the nearest position at which the deviation of the actual force from the ideal harmonic approximation starts to exceed 10% which is the conventional cutoff threshold,[8,9] represented by the vertical red dashed line). (b) The changing axial force curve shape upon rotation of the same rutile TiO_2 cylinder in (a) from θ = 0° to θ = 45° (with the rotation angle θ as defined in eq 1 from the main text). In this range, the deviation of z_{eq} is almost negligible (~6 nm) compared to the cylinder height (1 μm). As this behavior is similar to other cylinder dimensions as well, it is still valid to calculate the maximum optical torque (which occurs at θ = 45°) with z_{eq} obtained at θ = 0° (Figure 2c and Supporting Information, Figure S9). (c) The map of z_{eq}. For each black colored pixel, z_{eq} does not exist (i.e., the axial force curve has no x-intercept) and hence 3D-trapping is not possible for cylinders of the corresponding dimensions. We do not calculate radial trapping parameters at these positions, since we are interested in 3D-trappable cylinder dimensions only. For 3D-trappable

cylinder dimensions, the radial trapping parameters are calculated at z_{eq}. (d–f) The linear trap stiffness maps (κ_x, κ_y, and κ_z). (g–i) The linear trap strength maps ($F_{x,min}$, $F_{y,min}$, and $F_{z,min}$). (j–l) The linear harmonic potential regime maps (x_{hp}, y_{hp}, and z_{hp}). The blue curves are iso-height contours (500–4000 nm from left to right, with a step size of 500 nm). The resolution of the maps is $\Delta AR = 0.5$ and $\Delta d = 25$ nm. All calculations in panels (a)–(l) are performed assuming the vacuum wavelength of input beam $\lambda_o = 1064$ nm, a focus beam with objective lens NA = 1.2, an objective lens filling ratio $\alpha = \infty$, and a surrounding medium index $n = 1.33$. Except the cases of non-zero θ values in (b), the extraordinary axis of a nanocylinder coincides with the linear polarization direction of the input beam and therefore no rotation is assumed around any axis.

Additional Explanation of the Linear Trapping Parameters. In addition to the axial trap stiffness κ_z, various other axial trapping parameters should be considered when choosing appropriate cylinder dimensions for specific practical applications. For example, the axial trap strength $F_{z,min}$ can be used as a criterion to assess stable 3D trapping. If the axial trap strength of a cylinder is very weak, despite the trap itself having high axial stiffness (e.g., the nanocylinder with $d = 300$ nm and AR = 3.5), then such a particle is difficult to exploit since it will escape from the trap at the slightest external perturbation. Also, the extent of the linear axial force regime z_{hp}, combined with κ_z, provides information about the maximum applicable axial force under the assumption that the axial trap is a harmonic potential well (i.e., a linear Hookean spring). This information is valuable as proper trap calibration is easiest in this regime. The above definitions and reasoning apply similarly to radial trapping in x- and y-dimensions.

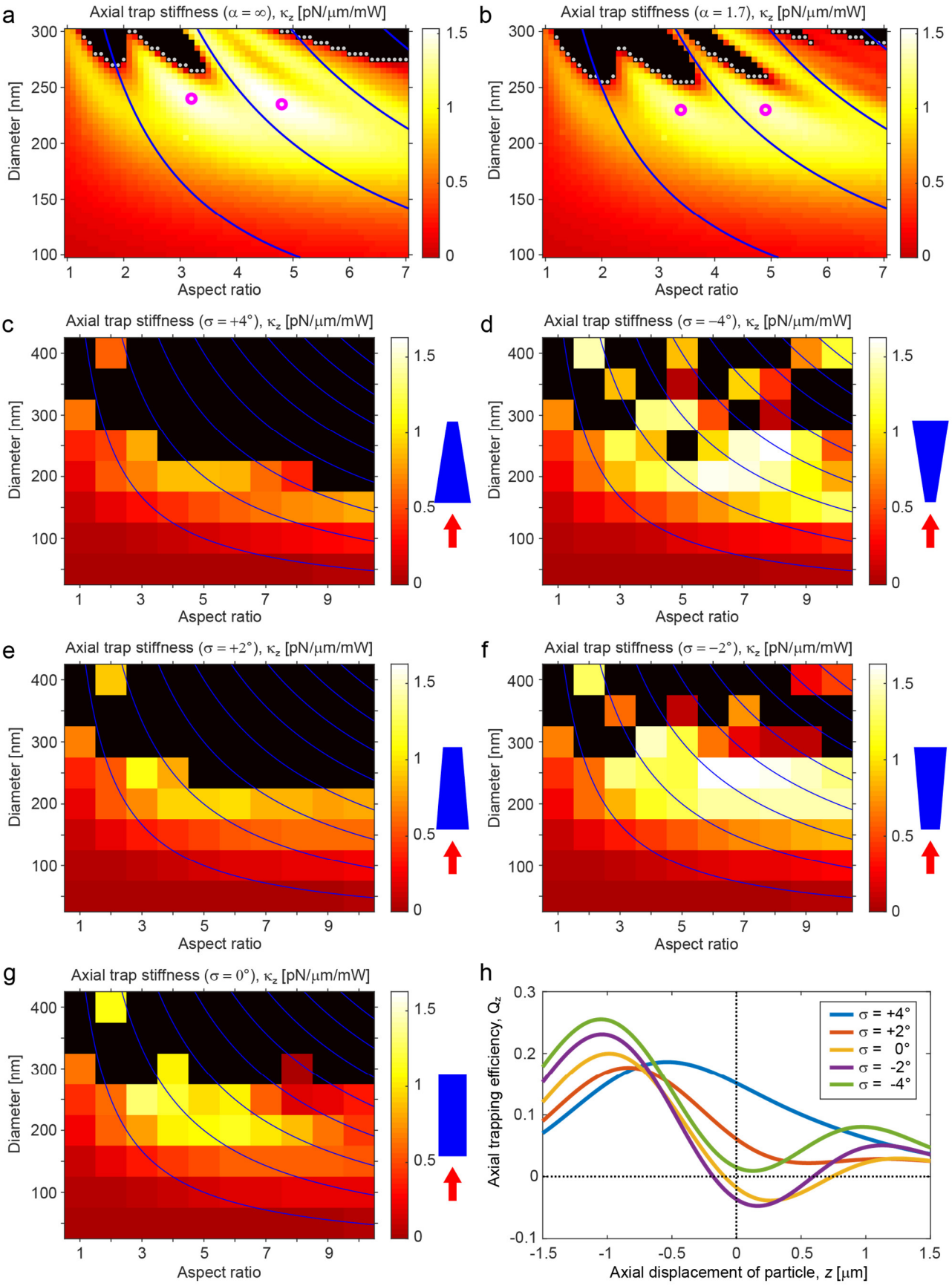

Figure S6. FEM-calculated maps of axial stiffness and curves of axial trapping efficiency for rutile TiO_2 nanocylinders with different objective lens aperture filling ratios and taper angles. (a, b) The FEM-calculated high-resolution maps of axial stiffness κ_z for rutile TiO_2 nanocylinders with (a) ideal ($\alpha = \infty$) and (b) measured ($\alpha = 1.7$; the same data as Figure 2a) objective lens aperture filling ratios. The calculated trappability threshold diameter d_{cal}* for each aspect ratio is displayed as a gray dot, and the magenta circles indicate the local maxima of stiffness.

Calculations based on the measured filling ratio (b) result in a narrower range of 3D-trappable cylinder diameters for aspect ratios between 1 and 5. The stiffness values at the local maxima are also reduced by ~10%, due to the less tight beam focusing for a smaller filling ratio. The blue curves are iso-height contours (500–2000 nm from left to right, with a step size of 500 nm). The resolution of the maps is $\Delta AR = 0.1$ and $\Delta d = 5$ nm. (c–f) κ_z maps of nanocylinders with a taper angle σ of (c) +4°, (d) −4°, (e) +2°, and (f) −2°, as a function of the aspect ratio and average diameter d_{av} (with ideal aperture filling ratio $\alpha = \infty$). The schematics to the right of the maps illustrate the taper angle (not to scale) and orientation of the cylinder body with respect to the laser beam propagation direction (red arrow). (g) κ_z map of perfectly straight nanocylinders (the same data as shown in panel (a) and Supporting Information, Figure S9a), displayed for straightforward comparison with the maps of tapered cylinders. The blue curves are iso-height contours (500–4000 nm from left to right, with a step size of 500 nm). The resolution of the maps is $\Delta AR = 1$ and $\Delta d = 50$ nm. (h) Axial trapping efficiency Q_z as a function of taper angle for a representative cylinder batch with $d_{av} = 250$ nm and AR = 5. All calculations in panels (a)–(h) are performed assuming the vacuum wavelength of input beam $\lambda_o = 1064$ nm, a focus beam with objective lens NA = 1.2, and a surrounding medium index $n = 1.33$.

Effects of Nanocylinder Taper Angle on Axial Trapping Properties. The dry etching process can result in nanocylinders with small taper angle (0–5°; T1–T8 and U1–U6 shown in Supporting Information, Figure S4 and Supporting Information, Table S1), and such geometrical asymmetry can alter the optical trapping characteristics.[10,11] To investigate this effect in rutile TiO_2 nanocylinders, we calculated axial trapping force F_z and then extracted axial stiffness κ_z for cylinders with taper angle σ of ±2° and ±4° while keeping the cylinder height and average diameter constant (thus, both the surface area and volume of the tapered cylinders are nearly the same as those of straight cylinders, allowing an unbiased comparison). For a tapered cylinder, two trapping orientations are possible with respect to the beam propagation direction. When the larger facet of a tapered cylinder is facing the source of the laser beam, the trappable regime shrinks and overall the trap stiffness decreases. This might be due to the increased light scattering at the larger entering surface of the particle, which destabilizes the trap. In contrast, when the tapered cylinder is flipped, and the smaller facet faces the beam source, the trappable regime expands and overall the trap stiffness increases. However, for each individual cylinder dimension, these changes are not proportional but nonlinearly correlated with the taper angle. For example, in the case of $d = 250$ nm and AR = 5 cylinder (Supporting Information, Figure S6h), changing taper angle from 0° to −2° enhances trap stiffness, but −4° taper renders the cylinder untrappable. Importantly, this result also advises us about what are the fabrication error-tolerant cylinder sizes, with which the particles can be always 3D-trapped even with small variations in taper angles. For example, $d = 200$ nm and AR = 4–6 cylinders can be 3D-trapped regardless of the taper angle variations of ±4°. For the fabricated and optically trappable rutile TiO_2 nanocylinder batches (T1–T8), taper angles are rather small (0.1–1.6°) and hence their trapping behaviors are expected to be similar to those of perfectly straight cylinders.

In case of applying the nanocylinders to measure tethered single biomolecules, the cylinder orientation with respect to the laser beam propagation direction is determined during cylinder fabrication. As our approach performs surface coating prior to cylinder cleavage, only the top side of cylinders before cleaving can be functionalized. Hence, the functionalized facet of a cylinder would be oriented to face the source of the laser beam, after coupling with a biomolecule that is tethered to the bottom of the flow cell. For a tapered cylinder, its trap stiffness can be substantially changed depending on the particle orientation (Supporting Information, Figure S6c–h). Therefore, one could tailor the functionalizable cylinder side to be a favorable one by fabricating cylinders with optimal taper angles, utilizing our fabrication protocol that enables control of taper angles in a wide range from negative to positive values.[12] Alternatively, the trap stiffness can be rendered to be less dependent on trapping orientations by minimizing the taper angle in fabrication (Supporting Information, Figure S2c,d).

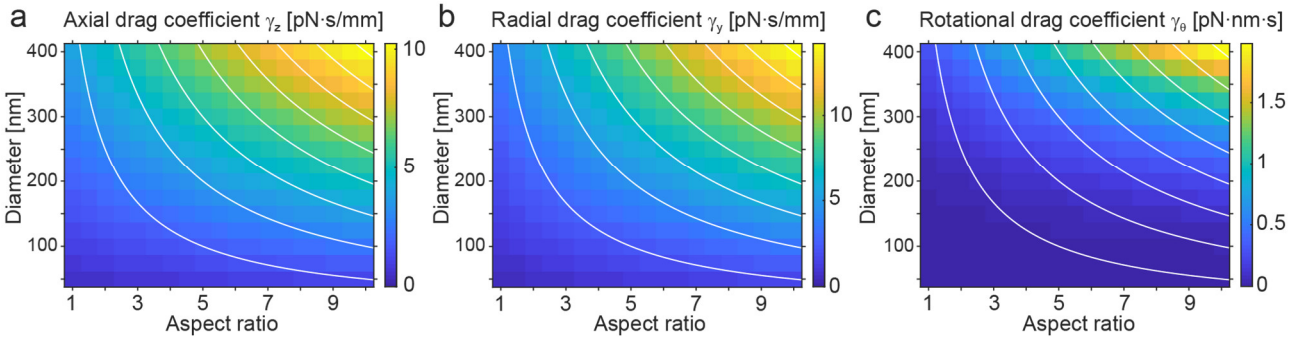

Figure S7. FEM-calculated translational and rotational hydrodynamic drag coefficients of nanocylinders. (a, b) The drag coefficients for translational movements of nanocylinders in water are FEM-calculated as a function of cylinder diameter and aspect ratio: (a) the axial linear drag coefficients (movement along the *z*-axis) and (b) the radial linear drag coefficients (movement along either the *x*- or *y*-axis). (c) The drag coefficients for rotational motion of nanocylinders (rotation about the *z*-axis). These rotational drag coefficients are used to calculate the maps of the maximum rotation frequency (Figure 2d and Supporting Information, Figure S9c,f,i). The resolution of the maps in panels (a)–(c) is $\Delta AR = 0.5$ and $\Delta d = 25$ nm. For Figure 2d in the main text, we used a drag map with higher resolution, $\Delta AR = 0.1$ and $\Delta d = 5$ nm. The white curves are iso-height contours (500–4000 nm from left to right, with a step size of 500 nm).

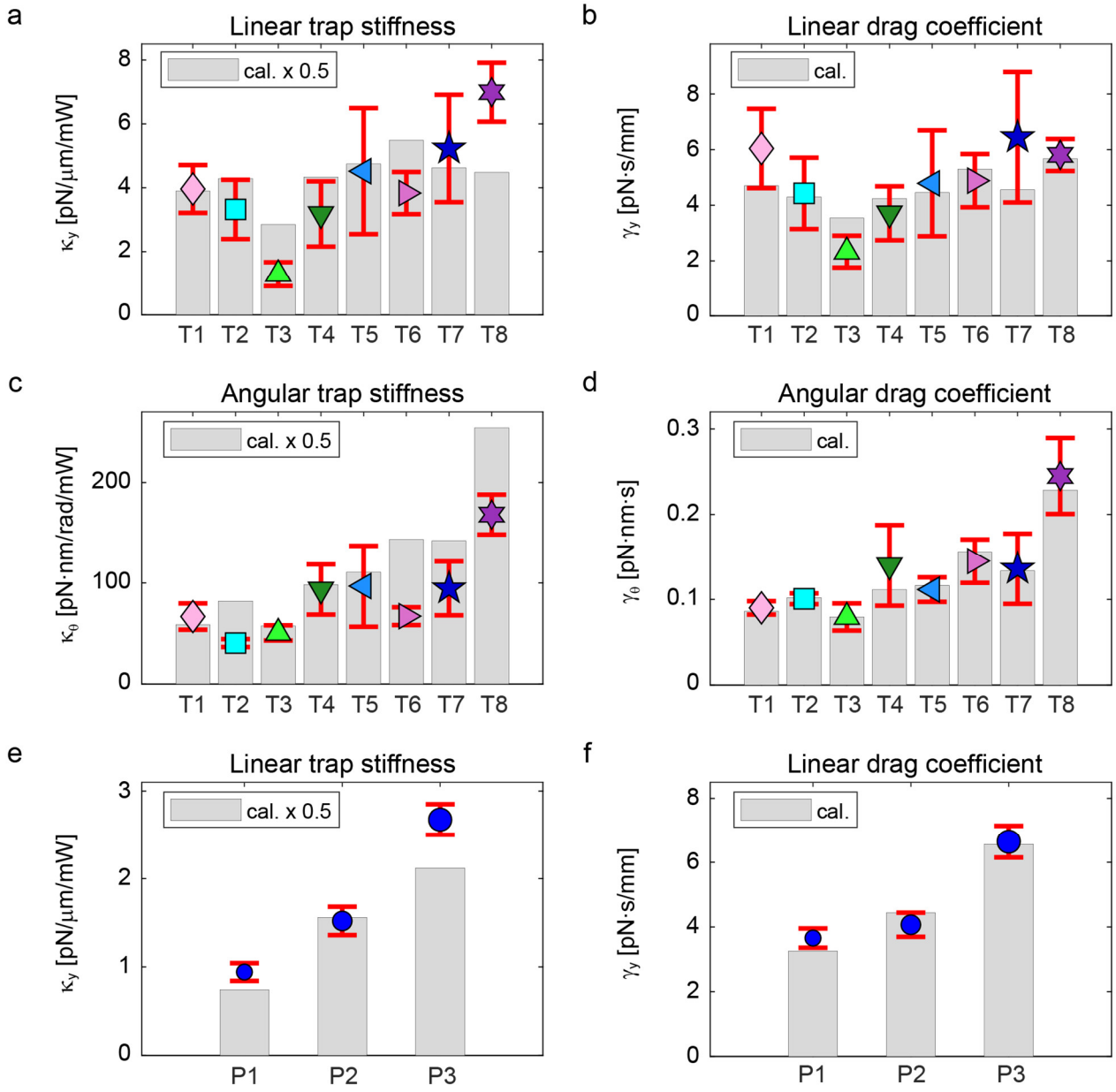

Figure S8. Comparison of experimentally and theoretically obtained stiffnesses and drag coefficients for trapping of rutile TiO_2 cylinders and PS spheres. For all trappable nanocylinder batches (T1–T8) and measured PS sphere batches (P1-P3), the trapping parameters obtained by both FEM calculations and OTW measurements are shown. The FEM calculations used the SEM-measured average dimensions for the cylinders, and the average diameter provided by the supplier for the spheres. (a) The linear trap stiffness (κ_y), (b) linear drag coefficient (γ_y), (c) angular trap stiffness (κ_θ), and (d) angular drag coefficient (γ_θ) of the rutile TiO_2 nanocylinders (summarized in Supporting Information, Table S2). (e) The linear trap stiffness (κ_y) and (f) linear drag coefficient (γ_y) of the PS spheres (summarized in Supporting Information, Table S3). In all panels, the gray bars indicate the FEM-calculated values, while the colored symbols (mean) and red error bars (SD) indicate the experimental values obtained by OTW-measurements of multiple particles per batch (N = 3–10). The FEM-calculated stiffness values (a, c, e) are scaled down by 50% for a direct comparison with experimental values (designated as cal. × 0.5). The mean ratios between OTW-measured and FEM-calculated values averaged over all batches are (a) for κ_y: 46% ± 16%, (b) for γ_y: 104% ± 22%, (c) for κ_θ: 38% ± 11%, and (d) for γ_θ: 103% ± 9% in case of rutile TiO_2 cylinders, and (e) for κ_y: 58% ± 7% and (f) for γ_y: 102% ± 8% (mean ± SD) in case of PS spheres. By averaging the ratios for the stiffnesses (a, c) and the drag coefficients (b, d) of rutile TiO_2 cylinders, respectively, we arrived at the values quoted in the main text (i.e., for κ: 42% ± 14% and for γ: 104% ± 17%). Overall, the calculations properly predict all observed trends in stiffness and drag for both rutile TiO_2 cylinders and PS spheres.

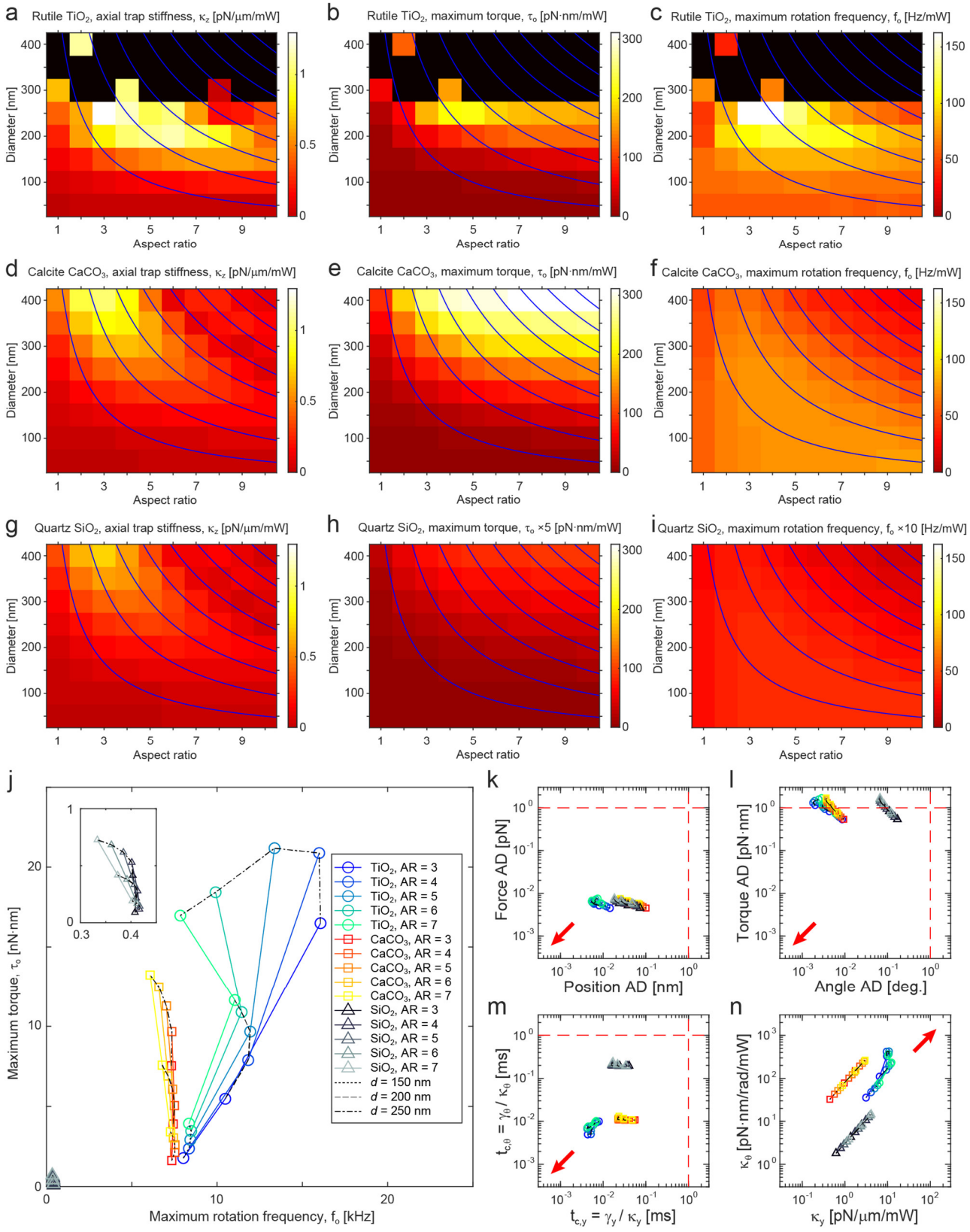

Figure S9. FEM-calculated linear and angular trapping parameters for different birefringent crystals. (a–i) For an unbiased comparison with the trapping parameters of (a–c) rutile TiO_2 nanocylinders, we performed similar FEM calculations for nanocylinders made of other birefringent crystals that are frequently used for OTW applications, including (d–f) calcite $CaCO_3$ and (g–i) quartz SiO_2. The calculated parameters are (a, d, g) the axial trapping stiffness κ_z, (b, e, h) the maximum torque τ_o, and (c, f, i) the maximum rotation frequency f_o. The maximum rotation frequency ($f_o = \tau_o/(2\pi\gamma_\theta)$) maps are obtained using the FEM-calculated angular drag coefficients γ_θ (Supporting Information, Figure S7). Each parameter is displayed with the same color scale across the maps of different materials. Within the calculated range of cylinder dimensions (d = 50–400 nm, AR = 1–10), only rutile TiO_2 has

dimensions that are not 3D-trappable (black pixels) due to its highest refractive index. Quartz SiO_2 has the smallest birefringence, and its angular parameters (τ_o and f_o) are very small (peak values are only 18.7 pN·nm/mW and 4.3 Hz/mW, respectively; for visibility, values are scaled up by (h) 5- and (i) 10-fold, respectively). The calculations are performed with λ_o = 1064 nm, NA = 1.2, $\alpha = \infty$, and n = 1.33. The blue curves are iso-height contours (500–4000 nm from left to right, with a step size of 500 nm). The resolution of the maps is ΔAR = 1 and Δd = 50 nm. (j–n) Using the FEM-calculated optical trapping parameters shown in panels (a)–(i) and drag coefficients (Supporting Information, Figure S7), the optical trapping performances of all three materials are predicted for cylinders with d = 150–250 nm and AR = 3–7. All symbols and colors are drawn according to the legend in panel (j). (j) The achievable torque-speed regime. The location of each symbol denotes the maximum torque and the maximum rotation frequency. The inset shows a magnified view of the quartz SiO_2 results. (k–l) Allan deviation (AD) analysis[13] to elucidate the (k) linear and (l) angular measurement precisions. All AD values are functions of signal averaging time and 1 s is assumed. (m) The linear and angular trap relaxation times that define the lower bounds of the temporal resolutions in measurements.[13] (n) The linear and angular trap stiffnesses. In panels (k)–(n), arrows indicate the preferable parameter regimes for the superior spatiotemporal resolutions in measurements. In panels (k)–(m), the vertical and horizontal red lines are the minimum desired spatiotemporal resolutions for diverse nanoscale experiments, particularly for single biomolecules (1 pN, 1 nm, 1 pN·nm, 1 degree, and 1 ms). In panels (j)–(n), note that all parameters except force AD and torque AD are dependent on input beam power. A value of 100 mW is assumed for parameters shown in panels (j)–(m), while the stiffnesses are normalized by power in panel (n).

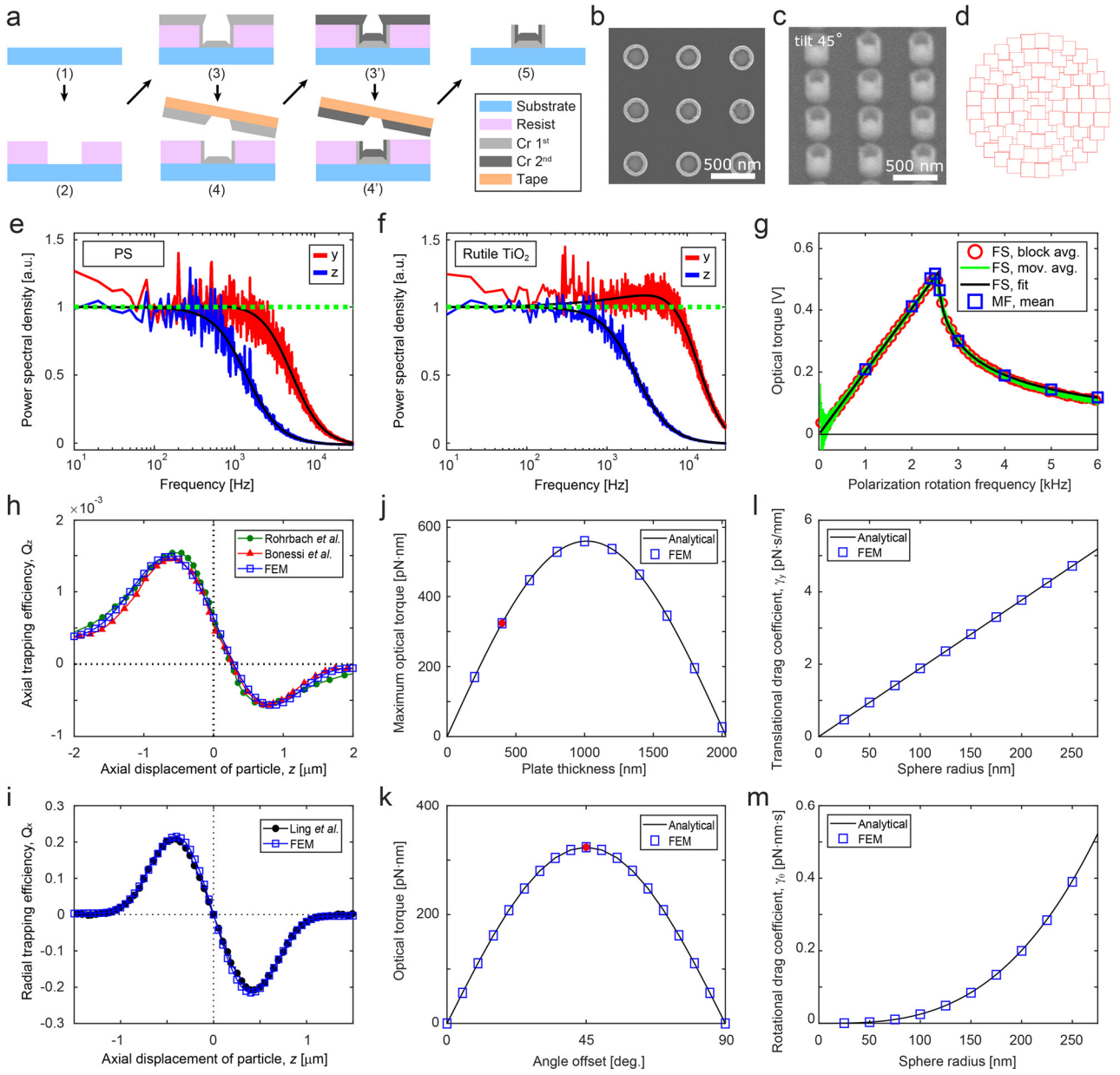

Figure S10. Improved methods for nanocylinder fabrication and trap calibration, and validation of FEM numerical models. (a–d) Our improvements in fabrication protocol, particularly in the etch mask and e-beam writing, for better control of the nanoscale geometry of rutile TiO_2 nanocylinders. (a) The fabrication steps for improved chromium (Cr) mask for rutile TiO_2 etching: (1) cleaning of a rutile TiO_2 substrate; (2) patterning of an e-beam resist layer (CSAR 62, ALLRESIST) on the substrate by e-beam lithography and resist development; (3) sputtering deposition (AC450, Alliance Concept) of the first Cr layer; (4) top Cr layer lift-off by attachment and subsequent removal of adhesive tape; (3'-4') sputtering and lift-off of the second Cr layer to permit a thicker Cr mask; (5) removal of e-beam resist by solvent (*N*-Methyl-2-pyrrolidone (NMP), GPR RECTAPUR (≥ 99.5%), VWR Chemicals). The resulting Cr mask has a very high base at center and a tall, thick surrounding wall. For the Cr mask shown here, the base has ~240 nm peak height and the surrounding wall is ~350 nm tall and ~40 nm thick. (b, c) The SEM micrographs of the Cr mask before etching, with (b) top-view and (c) 45° tilted view. (d) The improved e-beam writing pattern for disk-shaped Cr masks. This example is a disk pattern with d = 100 nm and beam step size of 10 nm. Each red square represents a position for an exposure of the e-beam. The e-beam writes in concentric rings from the center to the boundary, in a single sequence. (e, f) The effect of hydrodynamic memory on linear trap calibration of rutile TiO_2 nanocylinders. The OTW-measured (solid colored lines) and fitted (solid black lines) power spectral density (PSD) plots for linear trapping of (e) a PS sphere (batch P3, d = 746 nm) and (f) a rutile TiO_2 nanocylinder (batch T6, d_{av} = 216 nm, h = 1102 nm). The baseline amplitude (horizontal dashed green line) of each plot is normalized for a direct comparison. For the rutile TiO_2 cylinder in panel (f) only, the PSD plot from the radial trapping (along the y-axis) exhibits a resonance peak in the 1–10 kHz regime, resulting from the very high radial trapping stiffness that accompanies the hydrodynamic memory effect (described by the hydrodynamically corrected PSD function[9,14–16]). The PSD plots of the axial trapping of the rutile TiO_2 cylinder in

panel (f) and the axial and radial trapping of the PS bead in panel (e) do not show any hydrodynamic memory effect due to smaller trap stiffness values (described by the conventional Lorentzian PSD function[14]). Notably, we employed an improved position detection configuration in which radial and axial detection parts are separated.[17] (g) Our improved, rapid calibration method for torque-speed curve measurements in angular trap calibration of rutile TiO_2 nanocylinders. The conventional multi-frequency (MF) method of torque-speed curve measurement involves repeated torque measurements at multiple different polarization rotation frequencies (PRF).[4,5,18–20] In our frequency-sweep (FS) method, we sweep the PRF through a wide range within only a few seconds using a wavefunction generator (see Methods in the main text). In this example, we swept from 25 Hz to 7525 Hz in 6 s (i.e., 125 Hz/100 ms), and acquired the signal at a sampling frequency of 100 kHz. The measured signal can be converted to either block-averaged (red circles) or moving-averaged (green line) signal. The results are nearly identical and agree with the results from the MF method (blue squares; mean torque signal at steps of 1000 Hz across the measured PRF range and steps of 100 Hz around the peak position). Also, a good fit (black line) to the theoretical torque-speed equation[19] is possible. (h–m) We validated our FEM models by comparing them with analytical and other numerical treatments of PS spheres. (h, i) For linear momentum transfer, the force curves for optically trapped PS spheres obtained from our FEM calculation agree well with other numerical results (corresponding data points are extracted from the literature figures) for both (h) axial (with d = 200 nm sphere[21,22]) and (i) radial (with d = 1 μm sphere[23]) dimensions, when we use a beam with the same focal width as shown in the literature.[21–23] (j, k) For angular momentum transfer, we use the ideal configurations that were used to derive eq 1, assuming a birefringent plate of 300 nm × 300 nm cross-sectional area which is perpendicular to the beam propagation direction (Supporting Information, Text S1). We obtained FEM-calculated maximum torques as a function of either (j) the plate height h (with fixed offset angle θ = 45° to show maximal torque values only) or (k) the offset angle θ (with fixed particle height h = 400 nm as an example). As anticipated by eq 1, our results show that the optimal plate height of ~1 μm permits the maximal torque transfer as shown in panel (j). Also, for a fixed plate height (h = 400 nm), the maximal torque occurs at θ = 45° and only smaller or zero torques are generated at other angles, as shown in panel (k). The red dots in panels (j) and (k) are the same data point. (l, m) For hydrodynamic drag in aqueous solution, we compare our FEM models with the well-known analytical equations of spheres for both (l) translational ($\gamma_y = 6\pi\eta r$; η is the dynamic viscosity of water and r is the radius of sphere) and (m) rotational drag coefficients ($\gamma_\theta = 8\pi\eta r^3$).[24] The results of our FEM-based hydrodynamic calculations also agree excellently with the theory.

Advantages of Improved Cr Etch Mask Fabrication Protocols. Our previous Cr etch mask made by one-step Cr deposition by evaporation[12] is limited in the achievable maximum thickness of each mask, and the thickness at its edge is much smaller than that at its center. As a consequence, the edge of a mask erodes much faster than the center, resulting in a more tapered cylinder with longer etch time. The eroded edge also tends to be rough, so the cross section of etched cylinder is prone to be less circular. However, the improved Cr etch mask, with its reinforced edge and high base, ensures less tapered angles and a more perfect circular cross section even for extended etch times. Therefore, it is possible to fabricate high aspect ratio rutile TiO_2 cylinders with small taper angle, which function as optimal force and torque transducers (e.g., cylinder batch T6, h = 1102 nm, AR = 5.1, taper angle 0.2°; Supporting Information, Figure S4 and Table S1).

We also improved the design pattern for writing circular disks with e-beam lithography. The new pattern consists of a single writing sequence and requires much less time compared to the conventional pattern, which approximates a disk shape with multiple trapezoidal writing sequences. As a finite overhead time exists for each writing sequence, the gain in writing time becomes more evident when patterning larger areas. Our previous method also used single-sequence of writing per disk, consists of a single-pixel exposure with a defocused e-beam.[12] The defocused e-beam is faster over large arrays of disks (~0.5 h to pattern a circular area with a 4 mm radius). However, e-beam fluctuations can decrease the circularity of these disks. Our new method produces more circular disks and can cover the same area in ~1 h.

It is notable that such a decrease in the fabrication yield as a consequence of the patterning quality improvement is still acceptable for the purpose of nanocylinder trapping characterization. We pattern circles (i.e., cylinders) with 600 nm pitch on a circular patterning area with radius of ~4 mm on a rutile TiO_2 wafer of 1 cm x 1 cm size in ~1 h, resulting in ~140

million cylinders. At each cleaving process, we cleave cylinders over ~20% of the fabrication area on a wafer and collect the detached particles into ~100 μL of PBS buffer. This allows us to obtain a sufficiently high concentration (~0.5 pM, without considering the loss due to the nanocylinders adhered to the surface of the wafer or to the cleavage tool) to enable the localization of a nanocylinder within reasonable time. Considering the volume of our flow cell channel (~4 μL), the fabrication of a single wafer allows for more than 100 times separate experiments.

Advantages of Improved Force Measurement Method. The optical force is deduced from the particle position measurement. Previously, we detected 3D position (x, y, and z) of a particle using a single position sensitive detector (PSD) in our setup.[4,12] Here, we employed an improved method (as described in the Supporting Information of ref 17) for a more precise force detection. We use a non-polarizing beam splitter cube to relay a half of the output beam from the condenser lens to the PSD for the radial detection (x, y), while another half of the beam is guided to the photodiode (PD) for the axial detection (z). An iris is positioned before the PD and its opening is optimized to properly capture the Gouy phase[25] shift of the trapped particle. Although the PSD alone can also measure all three spatial coordinates (x, y, and z) of a trapped particle, this separated detection permits simultaneous optimization for both radial and axial measurements as they have conflicting requirements for iris opening.[17]

Advantages of Improved Torque-Speed Measurement Method. Using the conventional multi-frequency (MF) method, it is preferable to have a large number of data points (e.g., 50 Hz step size) for a better fit to the theory and a more precise detection of the peak position (for demonstration purpose, much less number of data points are taken than usual in the data set shown in Supporting Information, Figure S10g). However, for fast torque transducers like rutile TiO_2 nanocylinders, a smaller step size requires excessively long measurement times to switch between PRF values. The resulting torque-speed curves are prone to distortion by the long-term drift in the setup. Also, switching between many different frequencies is not practical, especially for setups with hardware that does not support automated PRF control. For example, in our setup, measurement of each torque signal costs ~1 min of overhead time due to the time required to manually switch the PRF and write the data to the hard disk. Hence, it requires at least ~1 h to acquire the data shown in Supporting Information, Figure S10g using the MF method with 100 Hz steps. As our frequency-sweep (FS) method allows torque measurement over a wide range of PRF values in just a few seconds, it is effectively free from the long-term drift in the setup. Hence, this method offers enhanced reliability and flexibility in torque spectroscopy. We note that both MF and FS methods detect torque using the same method based on the imbalance of the left- and right-circular polarization components measured by two PDs.

Supporting Tables

Table S1. SEM-measured dimensions of rutile TiO_2 nanocylinders. The SEM-measured dimensions of rutile TiO_2 nanocylinder batches (T1–T8, U1–U6) are listed. The parameters describing the cylinder geometry include the height (H), the averaged diameter (D_{av}), aspect ratio (AR = H/D_{av}), and the taper angle (σ). The parameter D_{av} is obtained by averaging the SEM-measured sidewall profile as can be seen in Supporting Information, Figure S4c, because the fabricated nanocylinder batches exhibit slight deviations from a perfectly straight sidewall. For the same reason, the taper angle is calculated from the slope of the linear fit to the averaged sidewall profile of each nanocylinder batch. Here, a positive (negative) taper angle means that the top flat surface (i.e., the surface protected by a Cr mask during plasma etching; designated by the yellow lines in Supporting Information, Figure S4a,b) is smaller (larger) than the bottom flat surface (i.e., mechanically cleaved position) of a cylinder. The values are obtained by measuring N = 5–15 different individual cylinders per batch. For each parameter, the displayed statistical values are the mean, the standard deviation (SD), and the relative standard deviation (RSD = SD/mean×100).

Parameter	**Unit**	**Trappable cylinders**								**Untrappable cylinders**					
		T1	**T2**	**T3**	**T4**	**T5**	**T6**	**T7**	**T8**	**U1**	**U2**	**U3**	**U4**	**U5**	**U6**
H (mean)	nm	**1071**	**816**	**578**	**766**	**830**	**1102**	**828**	**1115**	**664**	**1184**	**1062**	**1214**	**1048**	**1425**
H (SD)	nm	6	4	7	10	10	14	4	15	10	13	1	3	3	6
H (RSD)	%	0.6	0.4	1.1	1.4	1.2	1.3	0.5	1.3	1.5	1.1	0.1	0.3	0.3	0.5
D_{av} (mean)	nm	**166**	**199**	**205**	**214**	**215**	**216**	**229**	**256**	**259**	**259**	**299**	**293**	**326**	**354**
D_{av} (SD)	nm	6	4	5	12	12	16	9	10	6	7	15	9	9	9
D_{av} (RSD)	%	3.6	2.1	2.5	5.7	5.7	7.2	4	4.1	2.4	2.6	4.9	3	2.7	2.6
AR (mean)		**6.5**	**4.1**	**2.8**	**3.6**	**3.9**	**5.1**	**3.6**	**4.4**	**2.6**	**4.6**	**3.6**	**4.1**	**3.2**	**4.0**
AR (SD)		0.2	0.1	0.1	0.2	0.2	0.4	0.1	0.2	0.1	0.1	0.2	0.1	0.1	0.1
AR (RSD)	%	3.9	2.3	2.9	6.0	5.8	7.2	3.8	4.8	3.1	2.4	4.9	2.9	2.6	2.5
σ (mean)	deg.	**0.5**	**0.7**	**–1.6**	**0.2**	**–0.1**	**0.2**	**1.0**	**–0.2**	**4.8**	**0.4**	**0.5**	**2.7**	**0.6**	**3.9**
N		6	6	15	8	10	6	8	5	5	5	5	5	5	6

Table S2. OTW-measured and FEM-calculated optical trapping parameters of the 3D-trappable rutile TiO_2 nanocylinders. The linear and angular optical trapping parameter values for all 3D-trappable rutile TiO_2 nanocylinder batches (T1–T8) are listed. Both experimental (mean, standard deviation (SD)) and numerically calculated (cal.) results are displayed. The linear trapping properties include the radial drag coefficient (γ_y), the radial trap stiffness (κ_y), and the radial trap relaxation time ($t_{c,y}$). Similarly, the angular trapping properties include the angular drag coefficient (γ_θ), the angular trap stiffness (κ_θ), and the angular trap relaxation time ($t_{c,\theta}$). Note that the drag coefficients are independent of trapping beam power, while trap stiffnesses and trap relaxation times are not. Also, the calculated stiffnesses (linear or angular) represent the mean of those that result from the two possible trapping orientations. Regarding the angular trapping, the averaged maximal torque (τ_o) and angular speed (f_o) at 100 mW beam power (scaled from the actually used ~92 mW for rapid interpretation) are also shown. The experimental values are obtained by measuring N = 3–10 cylinders per batch.

Parameter	**Unit**	**T1**	**T2**	**T3**	**T4**	**T5**	**T6**	**T7**	**T8**
γ_y (mean)	pN·s/mm	**6.0**	**4.4**	**2.3**	**3.7**	**4.8**	**4.9**	**6.4**	**5.8**
γ_y (SD)	pN·s/mm	1.4	1.3	0.6	1.0	1.9	1.0	2.3	0.6
γ_y (cal.)	pN·s/mm	4.7	4.3	3.5	4.2	4.5	5.3	4.6	5.7
κ_y (mean)	pN/µm/mW	**4.0**	**3.3**	**1.3**	**3.2**	**4.5**	**3.8**	**5.2**	**7.0**
κ_y (SD)	pN/µm/mW	0.7	0.9	0.4	1.0	2.0	0.7	1.7	0.9
κ_y (cal.)	pN/µm/mW	7.8	8.6	5.7	8.7	9.5	11.0	9.2	9.0
$t_{c,y}$ (mean)	µs (at 100 mW)	**15**	**13**	**18**	**12**	**11**	**13**	**12**	**8**
$t_{c,y}$ (SD)	µs (at 100 mW)	5	5	7	5	6	3	6	1
$t_{c,y}$ (cal.)	µs (at 100 mW)	6	5	6	5	5	5	5	6
N_y		4	7	8	9	9	3	10	3
γ_θ (mean)	pN·nm·s	**0.09**	**0.10**	**0.08**	**0.14**	**0.11**	**0.15**	**0.14**	**0.24**
γ_θ (SD)	pN·nm·s	0.01	0.01	0.02	0.05	0.01	0.03	0.04	0.04
γ_θ (cal.)	pN·nm·s	0.09	0.10	0.08	0.11	0.12	0.16	0.13	0.23
κ_θ (mean)	pN·nm/rad/mW	**67**	**41**	**51**	**94**	**97**	**67**	**95**	**168**
κ_θ (SD)	pN·nm/rad/mW	13	4	8	25	40	9	27	20
κ_θ (cal.)	pN·nm/rad/mW	117	164	115	196	221	287	285	508
$t_{c,\theta}$ (mean)	µs (at 100 mW)	**14**	**25**	**16**	**15**	**12**	**22**	**14**	**15**
$t_{c,\theta}$ (SD)	µs (at 100 mW)	3	3	4	6	5	5	6	3
$t_{c,\theta}$ (cal.)	µs (at 100 mW)	7	6	7	6	5	5	5	4
τ_o	nN·nm (at 100 mW)	**3.3**	**2.0**	**2.5**	**4.7**	**4.8**	**3.4**	**4.7**	**8.4**
f_o	kHz (at 100 mW)	**5.9**	**3.2**	**5.1**	**5.3**	**6.9**	**3.7**	**5.5**	**5.5**
N_θ		4	7	7	9	8	3	7	3

Table S3. Dimensions and linear optical trapping parameters of the PS spheres. The dimensions and linear optical trapping parameter values for all measured PS sphere batches (P1–P3) are listed. For sphere diameter, the displayed statistical values are the mean, the standard deviation (SD), and the relative standard deviation (RSD = SD/mean×100). These values are provided by the supplier of the spheres. For linear optical trapping parameters, both experimental (mean, standard deviation (SD)) and numerically calculated (cal.) results are displayed. The trapping properties include the radial drag coefficient (γ_y), the radial trap stiffness (κ_y), and the radial trap relaxation time ($t_{c,y}$). Note that the drag coefficients are independent of trapping beam power, while trap stiffnesses and trap relaxation times are not. The experimental values are obtained by measuring N = 5–7 different individual spheres per batch.

Parameter	**Unit**	**P1**	**P2**	**P3**
D (mean)	nm	**370**	**505**	**746**
D (SD)	nm	15	8	2
D (RSD)	%	4.1	1.6	0.3
γ_y (mean)	pN·s/mm	**3.7**	**4.1**	**6.6**
γ_y (SD)	pN·s/mm	0.3	0.4	0.5
γ_y (cal.)	pN·s/mm	3.3	4.4	6.6
κ_y (mean)	pN/µm/mW	**0.9**	**1.5**	**2.7**
κ_y (SD)	pN/µm/mW	0.1	0.2	0.2
κ_y (cal.)	pN/µm/mW	1.5	3.1	4.2
$t_{c,y}$ (mean)	µs (at 100 mW)	**39**	**27**	**25**
$t_{c,y}$ (SD)	µs (at 100 mW)	5	4	2
$t_{c,y}$ (cal.)	µs (at 100 mW)	22	14	15
N		5	6	7

Supporting References

(1) Beth, R. A. Mechanical detection and measurement of the angular momentum of light. *Phys. Rev.* **1936**, *50*, 115–125.

(2) Friese, M. E. J.; Nieminen, T. A.; Heckenberg, N. R.; Rubinsztein-Dunlop, H. Optical alignment and spinning of laser-trapped microscopic particles. *Nature* **1998**, *394*, 348–350.

(3) Moothoo, D. N.; Arlt, J.; Conroy, R. S.; Akerboom, F.; Voit, A.; Dholakia, K. Beth's experiment using optical tweezers. *Am. J. Phys.* **2001**, *69*, 271–276.

(4) Pedaci, F.; Huang, Z.; van Oene, M.; Barland, S.; Dekker, N. H. Excitable particles in an optical torque wrench. *Nat. Phys.* **2010**, *7*, 259–264.

(5) La Porta, A.; Wang, M. D. Optical torque wrench: angular trapping, rotation, and torque detection of quartz microparticles. *Phys. Rev. Lett.* **2004**, *92*, 190801.

(6) Grießhammer, M.; Rohrbach, A. 5D-tracking of a nanorod in a focused laser beam – a theoretical concept. *Opt. Express* **2014**, *22*, 6114–6132.

(7) Tolić-Nørrelykke, S. F.; Schäffer, E.; Howard, J.; Pavone, F. S.; Jülicher, F.; Flyvbjerg, H. Calibration of optical tweezers with positional detection in the back focal plane. *Rev. Sci. Instrum.* **2006**, *77*, 103101.

(8) Jahnel, M.; Behrndt, M.; Jannasch, A.; Schäffer, E.; Grill, S. W. Measuring the complete force field of an optical trap. *Opt. Lett.* **2011**, *36*, 1260–1262.

(9) Jannasch, A.; Demirörs, A. F.; van Oostrum, P. D. J.; van Blaaderen, A.; Schäffer, E. Nanonewton optical force trap employing anti-reflection coated, high-refractive-index titania microspheres. *Nat. Photonics* **2012**, *6*, 469–473.

(10) Simpson, S. H.; Phillips, D. B.; Carberry, D. M.; Hanna, S. Bespoke optical springs and passive force clamps from shaped dielectric particles. *J. Quant. Spectrosc. Radiat. Transf.* **2013**, *126*, 91-98.

(11) Phillips, D. B.; Padgett, M. J.; Hanna, S.; Ho, Y. L. D.; Carberry, D. M.; Miles, M. J.; Simpson, S. H. Shape-induced force fields in optical trapping. *Nat. Photonics* **2014**, *8*, 400–405.

(12) Ha, S.; Janissen, R.; Ussembayev, Y. Y.; van Oene, M. M.; Solano, B.; Dekker, N. H. Tunable top-down fabrication and functional surface coating of single-crystal titanium dioxide nanostructures and nanoparticles. *Nanoscale* **2016**, *8*, 10739–10748.

(13) van Oene, M. M.; Ha, S.; Jager, T.; Lee, M.; Pedaci, F.; Lipfert, J.; Dekker, N. H. Quantifying the precision of single-molecule torque and twist measurements using Allan variance. *Biophys. J.* **2018**, *114*, 1970–1979.

(14) Berg-Sørensen, K.; Flyvbjerg, H. Power spectrum analysis for optical tweezers. *Rev. Sci. Instrum.* **2004**, *75*, 594–612.

(15) Franosch, T.; Grimm, M.; Belushkin, M.; Mor, F. M.; Foffi, G.; Forro, L.; Jeney, S. Resonances arising from hydrodynamic memory in Brownian motion. *Nature* **2011**, *478*, 85–88.

(16) Jannasch, A.; Mahamdeh, M.; Schäffer, E. Inertial effects of a small Brownian particle cause a colored power spectral density of thermal noise. *Phys. Rev. Lett.* **2011**, *107*, 228301.

(17) Friedrich, L.; Rohrbach, A. Surface imaging beyond the diffraction limit with optically trapped spheres. *Nat. Nanotechnol.* **2015**, *10*, 1064–1069.

(18) Gutiérrez-Medina, B.; Andreasson, J. O. L.; Greenleaf, W. J.; LaPorta, A.; Block, S. M., An optical apparatus for rotation and trapping. In *Methods in Enzymology*; Walter, N. G., Ed.; Academic Press: San Diego, CA, 2010; Vol. 475, pp 377–404.

(19) Inman, J.; Forth, S.; Wang, M. D. Passive torque wrench and angular position detection using a single beam optical trap. *Opt. Lett.* **2010**, *35*, 2949–2951.

(20) Huang, Z.; Pedaci, F.; van Oene, M.; Wiggin, M. J.; Dekker, N. H. Electron beam fabrication of birefringent microcylinders. *ACS Nano* **2011**, *5*, 1418–1427.

(21) Rohrbach, A.; Stelzer, E. H. K. Optical trapping of dielectric particles in arbitrary fields. *J. Opt. Soc. Am. A* **2001**, *18*, 839–853.

(22) Bonessi, D.; Bonin, K.; Walker, T. Optical forces on particles of arbitrary shape and size. *J. Opt. A: Pure Appl. Opt.* **2007**, *9*, S228–S234.

(23) Ling, L.; Zhou, F.; Huang, L.; Li, Z.-Y. Optical forces on arbitrary shaped particles in optical tweezers. *J. Appl. Phys.* **2010**, *108*, 073110.

(24) Leach, J.; Mushfique, H.; Keen, S.; Di Leonardo, R.; Ruocco, G.; Cooper, J. M.; Padgett, M. J. Comparison of Faxen's correction for a microsphere translating or rotating near a surface. *Phys. Rev. E* **2009**, *79*, 026301.

(25) Gittes, F.; Schmidt, C. F. Interference model for back-focal-plane displacement detection in optical tweezers. *Opt. Lett.* **1998**, *23*, 7–9.